

Position-Controlled Fabrication of Vertically Aligned Mo/MoS₂ Core–Shell Nanopillar Arrays

Maduro, Louis; Noordam, Marc; Bolhuis, Maarten; Kuipers, Laurens; Conesa-Boj, Sonia

DOI

[10.1002/adfm.202107880](https://doi.org/10.1002/adfm.202107880)

Publication date

2021

Document Version

Final published version

Published in

Advanced Functional Materials

Citation (APA)

Maduro, L., Noordam, M., Bolhuis, M., Kuipers, L., & Conesa-Boj, S. (2021). Position-Controlled Fabrication of Vertically Aligned Mo/MoS₂ Core–Shell Nanopillar Arrays. *Advanced Functional Materials*, 32(5), Article 2107880. <https://doi.org/10.1002/adfm.202107880>

Important note

To cite this publication, please use the final published version (if applicable).
Please check the document version above.

Copyright

Other than for strictly personal use, it is not permitted to download, forward or distribute the text or part of it, without the consent of the author(s) and/or copyright holder(s), unless the work is under an open content license such as Creative Commons.

Takedown policy

Please contact us and provide details if you believe this document breaches copyrights.
We will remove access to the work immediately and investigate your claim.



Pushing the boundaries
of chemistry?
It takes
#HumanChemistry

Make your curiosity and talent as a chemist matter to the world with a specialty chemicals leader. Together, we combine cutting-edge science with engineering expertise to create solutions that answer real-world problems. Find out how our approach to technology creates more opportunities for growth, and see what chemistry can do for you at:

evonik.com/career



Position-Controlled Fabrication of Vertically Aligned Mo/MoS₂ Core–Shell Nanopillar Arrays

Louis Maduro, Marc Noordam, Maarten Bolhuis, Laurens Kuipers, and Sonia Conesa-Boj*

The fabrication of 2D materials, such as transition metal dichalcogenides (TMDs), in geometries beyond the standard platelet-like configuration exhibits significant challenges which severely limit the range of available morphologies. These challenges arise due to the anisotropic character of their bonding van der Waals out-of-plane while covalent in-plane. Furthermore, industrial applications based on TMD nanostructures with non-standard morphologies require full control on the size-, morphology-, and position on the wafer scale. Such a precise control remains an open problem of which solution would lead to the opening of novel directions in terms of optoelectronic applications. Here, a novel strategy to fabricate position-controlled Mo/MoS₂ core–shell nanopillars (NPs) is reported on. Metal-Mo NPs are first patterned on a silicon wafer. These Mo NPs are then used as scaffolds for the synthesis of Mo/MoS₂ core/shell NPs by exposing them to a rich sulfur environment. Transmission electron microscopy analysis reveals the core/shell nature of the NPs. It is demonstrated that individual Mo/MoS₂ NPs exhibits significant nonlinear optical processes driven by the MoS₂ shell, realizing a precise localization of the nonlinear signal. These results represent an important step towards realizing 1D TMD-based nanostructures as building blocks of a new generation of nanophotonic devices.

1. Introduction

Vertically aligned 1D nanostructures have repeatedly demonstrated their relevance for applications ranging from biological sensors^[1–3] and single electron emitters^[4,5] to clean energy harvesting.^[6,7] Effectively deploying 1D nanostructures for such applications requires achieving an excellent and reproducible control of their sizes, shapes, and morphologies, as well as of

their position within the substrate. While these conditions have been fulfilled with astonishing degree of precision in the case of conventional semiconductor materials^[8,9] and heterostructures built upon them,^[10–13] the same level of control remains to be achieved for 2D materials such as those of the transition metal dichalcogenides (TMD) family.


Realising the size-, morphology-, and position-controllable fabrication of vertically-aligned 1D TMD nanomaterials would make possible opening several novel directions in terms of applications. Specifically, 1D TMD-based heterostructures which combine different materials would benefit from a greatly expanded portfolio of tunable properties, leading to emerging functionalities different from those found in the individual components. For instance, core–shell WO_x-WS₂ nanowires have been shown to outperform stand-alone 2D TMD-based capacitors due to the interplay between the conductive WO_x core and a WS₂ shell that favors fast ionic adsorption and transport.^[14] Likewise, MoO_x-MoS₂

nanowires exhibit an enhanced HER catalytic activity compared to 2D layers of MoS₂, thanks to the interplay between the conductive MoO_x core and the catalytically active MoS₂ shell.^[15,16]

However, achieving regular arrays of position-controlled vertically aligned 1D TMD-based heterostructures remains an open challenge. Until now, a variety of bottom-up approaches, that is, chemical vapor deposition growth,^[17,18] direct wet chemical synthesis,^[19,20] and solvothermal reactions,^[21] have been deployed for the fabrication of low-dimensional TMDs nanostructures. One significant difficulty facing these techniques when assembling 1D nanostructures based on TMD materials lies in the anisotropic (van der Waals out-of-plane and covalent in-plane) character of their bonding, which favors the formation of platelet-like structures when growing them using bottom-up approaches and thus limits the range of available morphological configurations.

Realizing the exciting potential of vertically-aligned 1D TMD-based heterostructures for technological applications thus clearly demands a reproducible, flexible, and size-, morphology-, and position-controllable fabrication strategy. With this motivation, here we develop a novel approach for the fabrication of metal/TMD core–shell 1D nanostructures based on the combination of top-down and bottom-up methods, and demonstrate its feasibility for the fabrication of vertically aligned Mo–MoS₂

L. Maduro, M. Noordam, M. Bolhuis, L. Kuipers, S. Conesa-Boj
Kavli Institute of Nanoscience
Delft University of Technology
Delft 2628CJ, The Netherlands
E-mail: s.conesa@tudelft.nl

 The ORCID identification number(s) for the author(s) of this article can be found under <https://doi.org/10.1002/adfm.202107880>.

© 2021 The Authors. Advanced Functional Materials published by Wiley-VCH GmbH. This is an open access article under the terms of the Creative Commons Attribution-NonCommercial-NoDerivs License, which permits use and distribution in any medium, provided the original work is properly cited, the use is non-commercial and no modifications or adaptations are made.

DOI: 10.1002/adfm.202107880

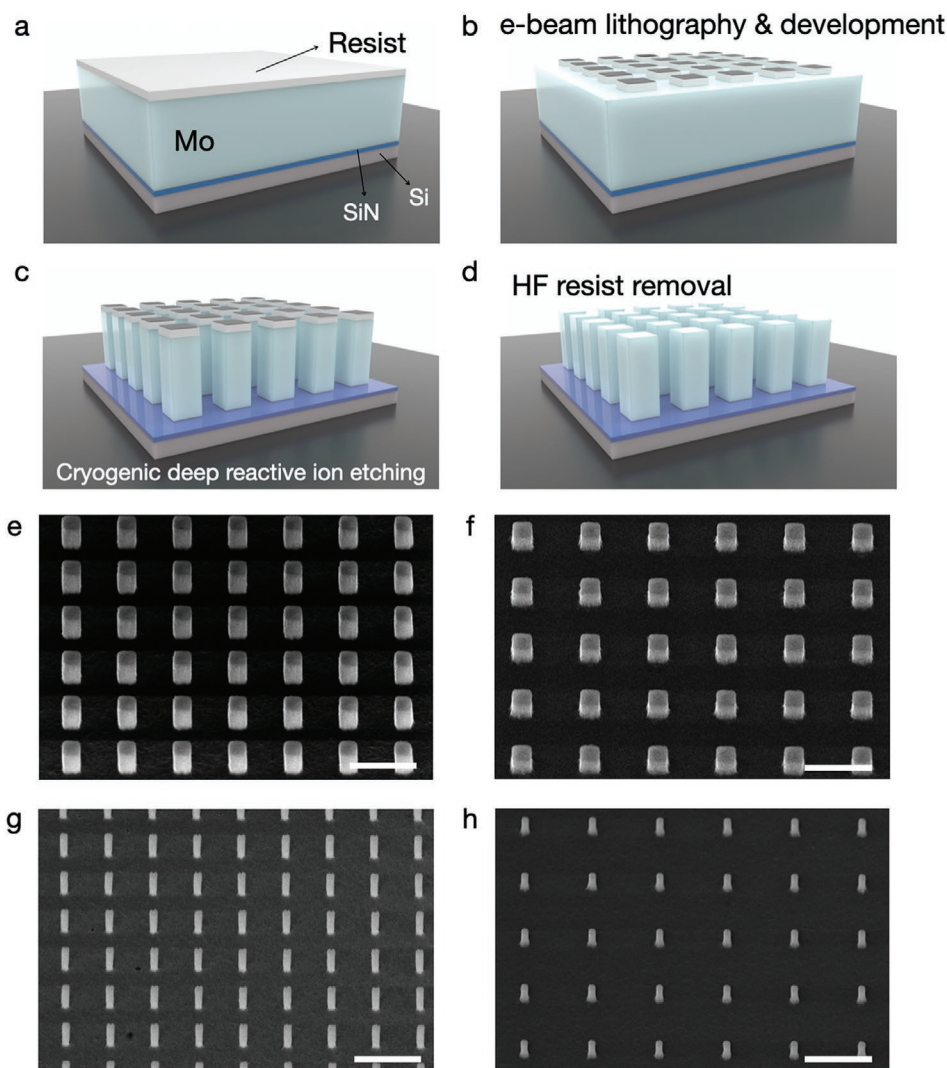


Figure 1. a–d) Workflow of the strategy adopted for the fabrication of Mo-based nanopillar (NP) arrays. e–h) SEM images of square cross-section Mo-based NP arrays. Panels (e) and (g) display NPs with height of 500 nm, while those in (f) and (h) exhibit a height of 350 nm. The width of the NPs varies from 250–300 nm in (e) and (f) to 100–150 nm in (g) and (h). The scale bars are 1 μm .

core-shell heterostructures denoted as nanopillars (NPs). Our strategy builds upon the two-step process,^[22] and is based on the sulfurization of the as-prepared Mo NPs in a chemical vapor deposition (CVD) setup^[22,23] leading to core-shell Mo/MoS₂ 1D NPs. State-of-the art transmission electron microscopy (TEM) combined with high-resolution electron energy-loss spectroscopy (EELS) is used to confirm the structural nature of the as-fabricated Mo/MoS₂ core-shell NPs. Our analysis is complemented with nonlinear optical measurements which demonstrate clear evidence of enhanced second order processes generated entirely by the MoS₂ shells of individual NPs.

This nonlinear response is found to be qualitatively similar to that of reference MoS₂ flakes, with the NP configuration offering key advantages such as precise localisation of the nonlinear signal at the wafer scale.

The results of our work demonstrate that vertical core-shell 1D nanostructures can also be fabricated with TMD materials with a high degree of morphology- and position-control. While here we have considered Mo/MoS₂ NPs as a proof-of-concept,

our approach is fully general and can be deployed for other TMD materials such as WS₂ or MoSe₂.

2. Results

2.1. Fabrication of Mo-Based NP Scaffolds

Figure 1 illustrates the workflow of the strategy adopted for the fabrication of the Mo-based nanopillar (NP) arrays, based on deep-reactive ion etching at cryogenic temperatures. These Mo NP arrays will provide the scaffolds for the subsequent Mo/MoS₂ core-shell NPs. We first deposit a low-stress Si₃N₄ layer followed by sputter-deposition of a Mo metal layer. The height of the resulting Mo NP scaffold can then be adjusted by varying the thickness of the initial sputtered Mo-metal layer. Here, the thickness of the Mo-metal layer is varied between 350 nm and 880 nm. Afterward, a spin coating of hydrogen silsesquioxane negative tone resist is carried out on top, as indicated in Figure 1a,

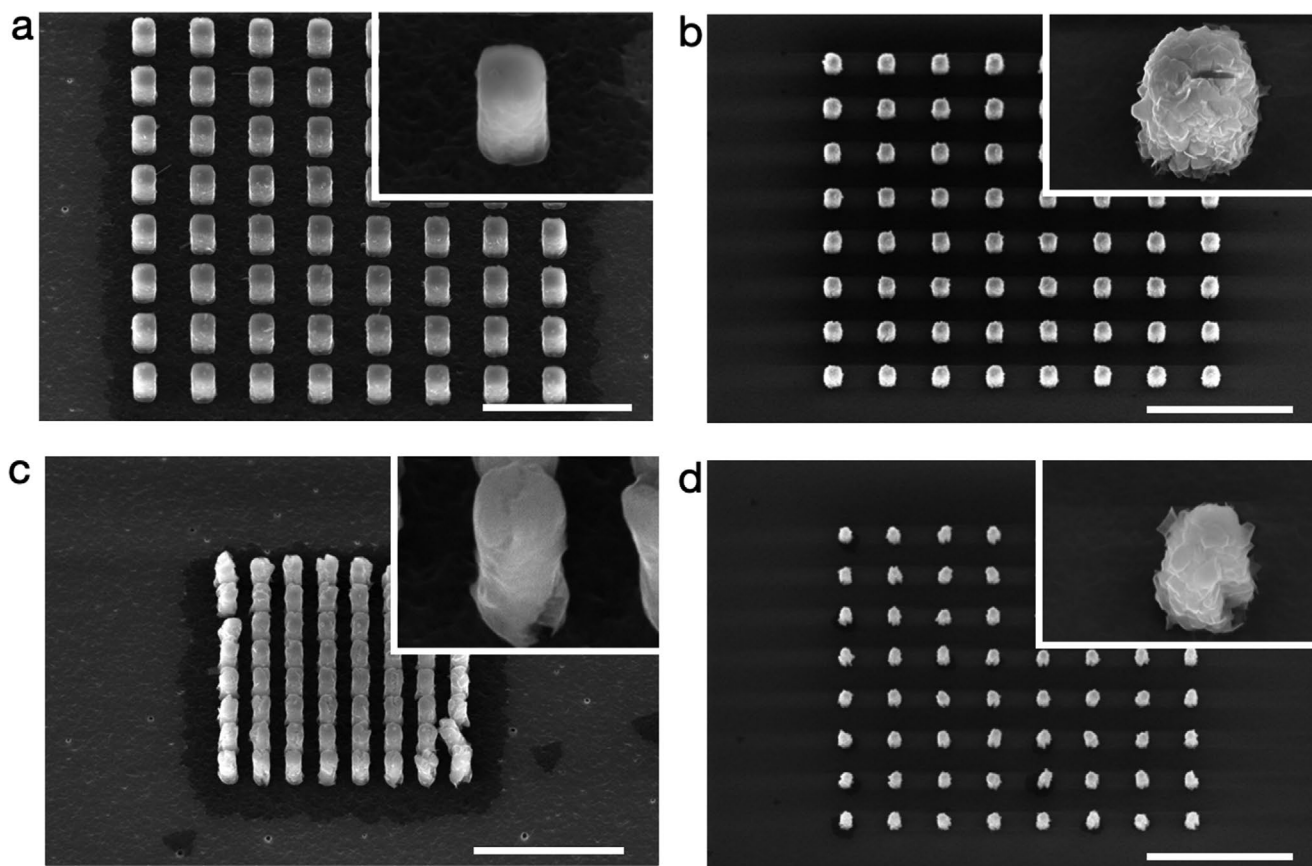


Figure 2. SEM images of the sulfurized square Mo-based NP arrays. Panels (a) and (c) correspond to NP sulfurized during 5 min, while the NPs in (b) and (d) are sulfurized during 7.5 min. Each of these arrays corresponds to a different width of the original Mo NPs, namely 300 nm (a,b) and 150 nm (c,d). The scale bars in (a,c) are 2 μm and in (b,d) are 5 μm .

and subsequently baked in two consecutive steps of 150°C and 220°C for 2 min each. Next, the desired design of the array, including dimensions, cross-section shape, and pitch are then written using electron beam lithography (Figure 1b). After cryogenic deep reactive ion etching in a SF_6/O_2 gas mixture, Figure 1c, and the removal of the remaining resists with HF, the etched Mo-metal layer exhibits the desired design, leading to the end result shown in Figure 1d. Further details of the Mo NPs fabrication process can be found in Section S1, Supporting Information.

Figure 1e–h displays scanning electron microscopy (SEM) images of the square cross-section Mo-based NP arrays characterized by widths varying from 250–300 nm (Figure 1e,f) to 100–150 nm (Figure 1g,h). The height of these Mo NPs is around 500 nm in Figure 1e,g and 350 nm in Figure 1f,h. The same strategy has been successfully deployed for the design and engineering of Mo NP arrays exhibiting different cross-sectional geometries,^[24] specifically for triangular, hexagonal, and circular cross-sections (see Figure S1, Supporting Information).

2.2. Synthesis and Characterization of Mo/MoS₂ Core–Shell NP Arrays

Inspired by the Mo seed-mediated MoS₂ growth,^[22] we now adopt the same strategy by using the Mo-based NP array as scaffolds to seed the growth of Mo/MoS₂ core/shell nano-

pillars arrays. The synthesis of the Mo/MoS₂ core/shell nanopillars is carried out in a chemical vapor deposition (CVD) system under a sulfur-rich environment. The sulfurization takes place at ambient pressure. A reaction temperature of 650°C and an Ar gas flow of 150 sccm are used. Under these conditions, the outer surface of the Mo NP turns out to be MoS₂ resulting in the formation of core–shell Mo–MoS₂ NPs.

Figure 2 displays SEM images of the sulfurized Mo-based NP arrays. Three sulfurization times were considered, namely 5, 7.5, and 10 min. Figure 2a,c corresponds to Mo NPs sulfurized during 5 min while Figure 2b,d to 7.5 min. The pitch in Figure 2a–d is 500, 1500, 300, and 1500 nm, respectively. The presence of MoS₂ on the sulfurized NPs is confirmed by means of Raman spectroscopy measurements, see Figure S2, Supporting Information. Specifically, these measurements find two Raman modes located at 381 cm^{-1} and at 407 cm^{-1} , corresponding to the in-plane E_{2g}^1 and out-of-plane A_{1g} Raman modes of trigonal prismatic 2H-MoS₂, respectively.

For reaction times of 5 min, it is found that the MoS₂ shell follows reasonably close the shape of the original Mo scaffolds, while for 7.5 min their surfaces are somewhat less defined. The presence of surface roughness for sulfurization times of 7.5 min or longer can be traced back mainly to the energy accumulation which takes place in the MoS₂ shell during sulfurization. Indeed, the higher the amount of Mo amount consumed, the thicker the MoS₂ shells become, and hence the

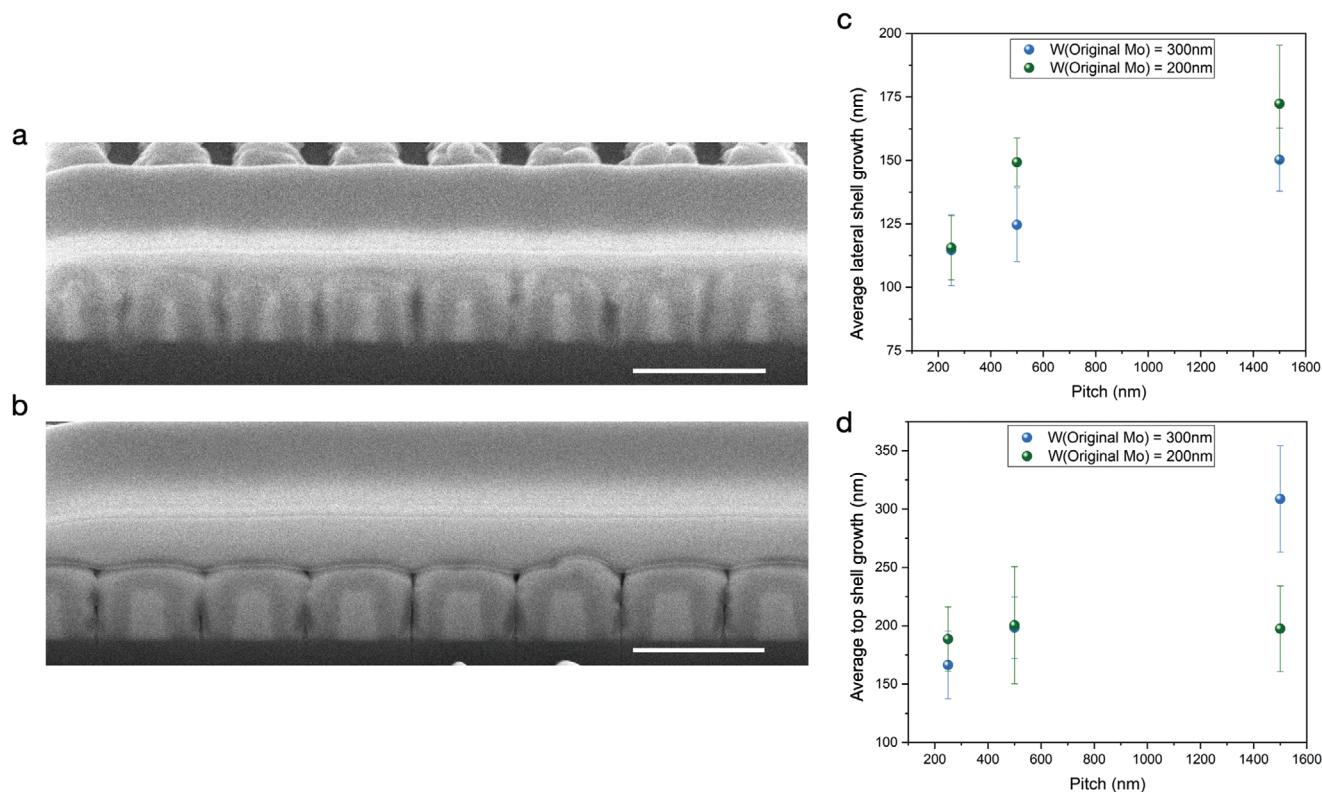


Figure 3. a–b) SEM images of FIB cross-sections carried out for two different NP arrays. The original Mo NP widths are 200 nm (a) and 300 nm (b), with a pitch value of 500 nm and a sulfurization time of 7.5 min for both arrays. The scale bar is 1 μm. The lighter (darker) contrast indicates the Mo core (MoS₂ shell). c,d) Average thickness of the MoS₂ shell growth (evaluated over 10 NPs in each case) in the lateral (c) and top sides (d). The error bar indicates the standard deviation over the measured NPs. The increase in the MoS₂ shell growth for larger pitches highlights the effect of the competitive growth-regime between nearby NPs.

energy accumulated at the shell increases accordingly.^[25,26] This energy is released by the separation of part of the MoS₂ layers, giving place to the roughness that is observed. This trend is also observed for those Mo NPs that have been sulfurized for 10 min (see Figure S3). Furthermore, after sulfurization, the NPs from the arrays with pitch values equal or smaller than 500 nm exhibit a marked horizontal MoS₂ growth localized at their base, leading to a large uniform film at the base of the whole array as displayed in Figure 2a,c.

SEM images of focus ion beam (FIB) cross-sections performed for two different NP arrays are displayed in Figures 3a,b. The lighter (darker) contrast highlights the Mo metal core (MoS₂ shell). The original Mo NP widths are 200 and 300 nm for Figures 3a and 3b, respectively, with a pitch value of 500 nm and a sulfurization time of 7.5 min for both arrays. The information extracted from these cross-sectional SEM images is used to determine the thickness of the MoS₂ shell in both the lateral and top sides for the NP arrays considered. By averaging over 10 NPs in each of these two arrays, one can assess the dependence of the MoS₂ shell thickness along the lateral and top sides of the NP as a function of the pitch, displayed in Figure 3c and 3d, respectively. On the one hand, the thickness of the MoS₂ shell in the lateral side appears to be larger as the pitch is increased, with the NPs with original Mo width of 200 nm exhibiting the thicker shell. One possible explanation for this trend is that the direct flux of the sulfur precursor

impinging on the Mo NP sidewalls is one of the main pathways contributing to the growth of MoS₂. This contribution decreases when the distance between Mo NPs (pitch) is reduced due to the competition between nearby NPs. Concerning the growth of the MoS₂ shell along the top side, we observe that the thickness of the MoS₂ shell does not vary with the pitch of the Mo NPs for a original width of 200 nm. For the NPs with larger original width instead (300 nm), the shell thickness increases with respect to the pitch.

Figure 4 displays the results of the high-resolution transmission electron microscopy (HR-TEM) analysis of a FIB cross-section carried out on a core-shell Mo/MoS₂ NP synthesized with a reaction time of 7.5 min. First of all, Figure 4a displays a low-magnification bright-field TEM image of the cross-section TEM lamella. The difference in contrast highlights the core-shell morphology of the NPs, with the darker contrast of the Mo-metal core surrounded by the brighter one of the MoS₂ shell. The presence of Mo metal in the core and of MoS₂ in the shell of the NPs is further confirmed by the EELS analysis reported in Figure S4, Supporting Information, which identifies the characteristic bulk plasmon peaks of metallic Mo (in the core) and of MoS₂ (in the shell region). Then, Figure 4b–e show HR-TEM images acquired at different positions of the Mo/MoS₂ interface in the same NP, namely at the top for Figure 4b and at the sidewalls for Figure 4c,d. This analysis demonstrates how the majority of the MoS₂ layers (basal

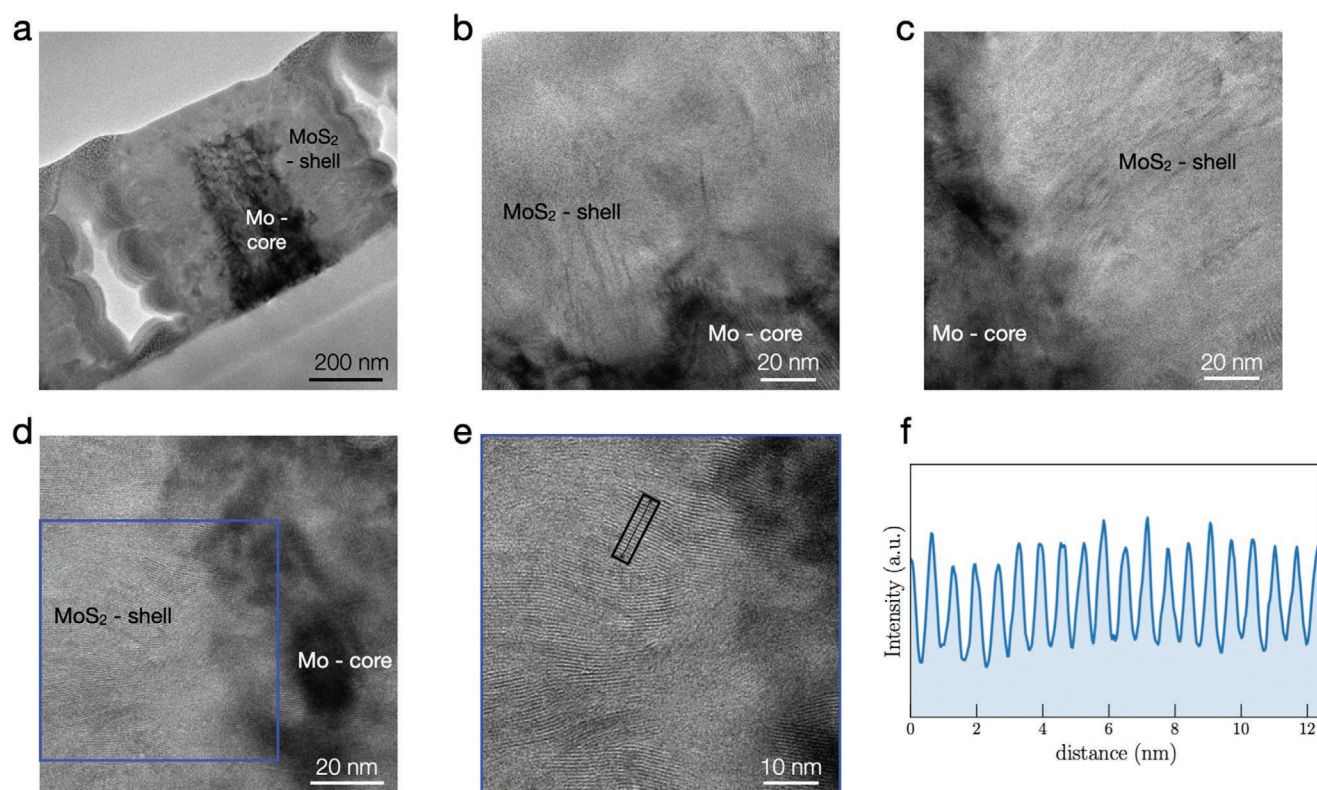


Figure 4. HR-TEM analysis of a FIB cross-section carried out on a core-shell Mo-MoS₂ NP synthesized with a reaction time of 7.5 min. a) Low-magnification HR-TEM image where the dark (light) contrast highlights the Mo-core (MoS₂ shell). b–d) High-resolution images of the top (b) and sides (c,d) of the NP revealing how the MoS₂ layers grow perpendicular to the Mo core surface. e) Magnification of the region marked with a blue square in (d). f) Intensity line profile acquired over the black rectangle in (e) quantifying the spacing between the MoS₂ layers.

planes) grow perpendicularly to the sidewalls of the Mo NP core, a configuration which increases the number of exposed edge sites. A high density of MoS₂ exposed edge sites is known to be advantageous for many applications, due to the high reactivity that these edge sites exhibit. The distance between adjacent MoS₂ layers is determined from an intensity line profile (Figure 4f) recorded on the black rectangle in Figure 4e from the lateral region of the shell. The interlayer distance is measured to be around 0.64 nm, consistent with the spacing for the basal planes of hexagonal 2H-MoS₂ nanostructures.^[22] Furthermore, we find that the orientation of the MoS₂ layers in the shell behaves in a similar fashion for the different reaction times; the reaction time mostly dictates the amount of Mo consumed and transformed into MoS₂, see Figure S3b,c, Supporting Information.

2.3. Nonlinear Optical Response

2D materials have generated ample attention because of the nonlinear optical (NLO) response induced by their characteristic inversion symmetry breaking.^[27,28] As an illustration, second-order nonlinear optical processes have been reported in MoS₂ flakes,^[29] where it is found that their intensity increases exponentially when decreasing the number of layers. This indicates that MoS₂ monolayers should be the most efficient thickness in order to enhance second-order processes.

With this motivation, here we characterise in detail the NLO response of the Mo/MoS₂ core-shell NPs. For these measurements, NP arrays with two different values of the pitch (400 and 1500 nm) and of the original Mo NP widths (150 nm and 300 nm) are considered. For all samples, the optical setup (e.g. laser powers) is identical to ensure a consistent comparison. A schematic of the optical setup adopted is displayed in Figure 5a. Two different color ultrashort laser pulses with wavelengths of 775 and 1200 nm are used, with a pulse duration of 150 fs at a 80 MHz repetition rate and a linear horizontal polarization. The average power of the laser pulses is set to 0.8 and 1.9 mW for the 1200 and 775 nm pulses, respectively. A linear translation stage in the 1200 nm beam path is used to synchronize the laser pulses. The two different color laser beams are then combined using a dichroic mirror and focused at the sample using a microscope objective (Olympus UPL- SAPO, NA = .95) at a perpendicular angle. In this way, both laser pulses are spatially and temporally overlapped to generate the nonlinear signals. The generated nonlinear signals are collected using the same microscope objective. After removing the reflected fundamental light with low-pass filters, the nonlinear emission is measured using a spectrometer (Princeton Instruments, Acton 2300I). Figure 5b displays the optical image acquired on the Mo/MoS₂ core-shell NP array with pitch sizes of 1500 and 300 nm of original Mo NP width.

Figure 5c shows the nonlinear optical response recorded on Mo/MoS₂ NPs from the array with 400 nm pitch and 300 nm

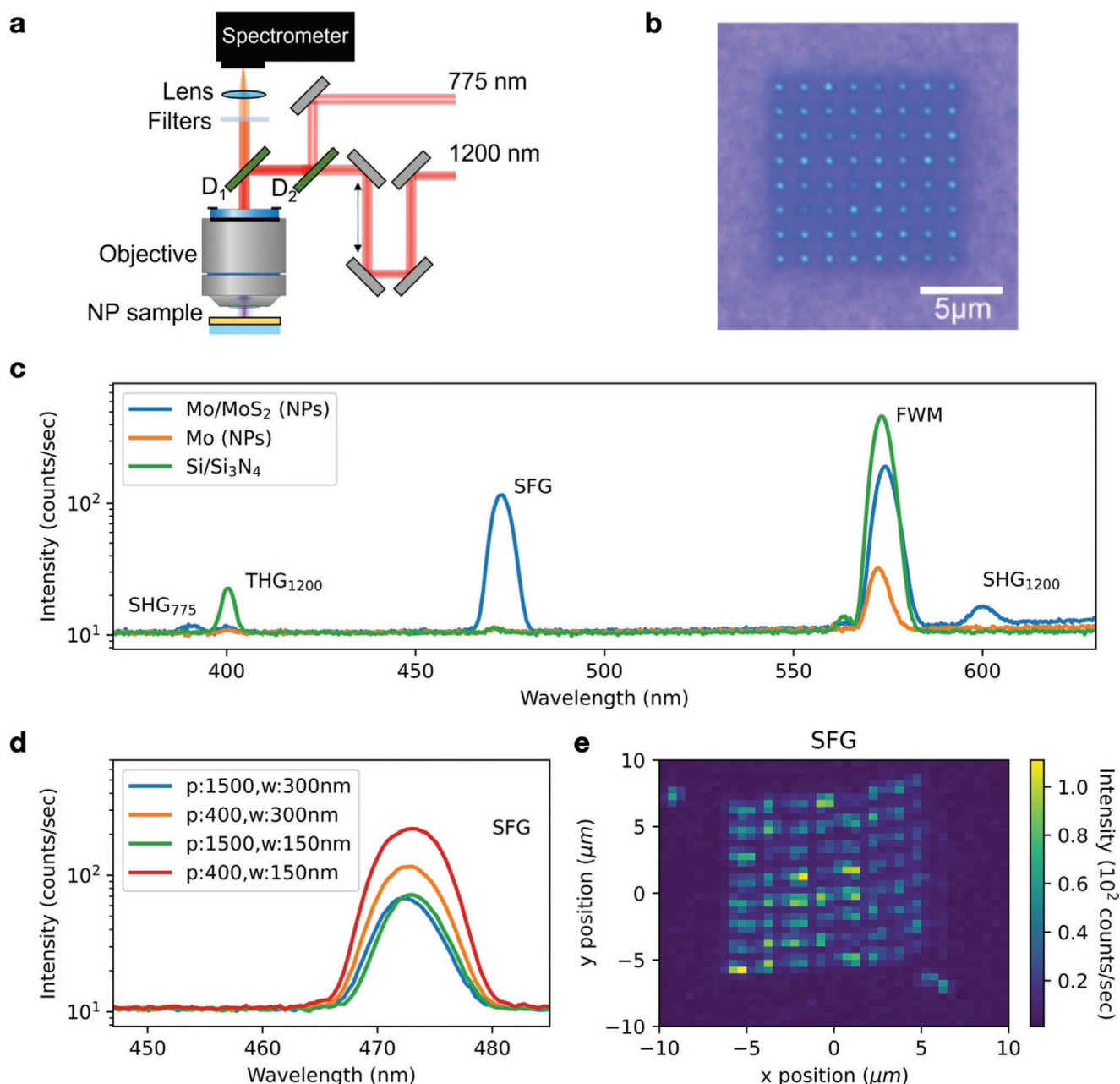


Figure 5. Overview of the nonlinear optical measurements acquired on the core-shell Mo/MoS₂ NPs. a) Schematic of the optical setup. b) Optical image of the Mo/MoS₂ NP array with pitch of 1500 nm and Mo NP width of 300 nm. c) The acquired nonlinear optical response on Mo/MoS₂ NPs from the array with 400 nm pitch and 300 nm width. The response of the Mo/MoS₂ NPs (blue) is compared with that of the corresponding original (pre-sulfurization) Mo NPs (orange) and with the response from the Si/Si₃N₄ substrate (green). d) SFG signal for the Mo/MoS₂ NPs corresponding to arrays with different pitches and Mo NP widths. e) Raster scan image of the same SFG signal over the NP array displayed in (b).

width. The response of these NPs is compared with that of the corresponding original (pre-sulfurization) Mo NPs and from the Si/Si₃N₄ substrate. Five peaks can be identified in the Mo/MoS₂ NP spectrum, which can be attributed to the following processes: second-harmonic generation (SHG) where $\omega_{\text{SHG}} = 2\omega_{1200}$ and $\omega_{\text{SHG}} = 2\omega_{775}$, third-harmonic generation (THG) where $\omega_{\text{THG}} = 3\omega_{1200}$, sum-frequency generation (SFG) where $\omega_{\text{SFG}} = \omega_{775} + \omega_{1200}$, and four-wave mixing (FWM) where $\omega_{\text{FWM}} = 2\omega_{775} - \omega_{1200}$. The Mo/MoS₂ NP spectrum exhibits large

signals arising from the second-order processes, SHG and SFG, which are essentially absent from both the substrate and the original Mo NPs. The fact that second-order nonlinear signals do not appear in the Mo NP reference confirms that these are entirely generated by the MoS₂ shells. Concerning the third-order nonlinear signals, FWM and THG, these are already present in the substrate, though interestingly the FWM peak is also enhanced in the Mo/MoS₂ NPs as compared to the Mo NP reference. Furthermore, we have compared this nonlinear

response of the Mo/MoS₂ NPs with that on a reference baseline consisting of a monolayer MoS₂ flake, representing the same material under a different configuration, for identical laser conditions. As demonstrated by Figure S5, Supporting Information, the nonlinear spectra from the Mo/MoS₂ NPs and from the horizontal MoS₂ flake exhibit the same qualitatively features, with the former offering precise localisation as key advantage.

Motivated by the observation of second-order nonlinear signals in the Mo/MoS₂ NPs, we study their dependence with the array pitch size and width of the original Mo NPs in Figure 5d. The SFG signal is compared between Mo/MoS₂ NPs from arrays with different representative values of the pitches (400 and 1500 nm) and Mo NP widths (150 and 300 nm), in all cases corresponding to 10 min of sulfurization time. For pitches of 400 nm, an enhanced intensity is observed for the thinner NPs with original Mo NP width of 150 nm. We note that here the contribution from different NPs may partially overlap due to the spatial resolution of the measurement (≈ 500 nm) arising from the finite spot size of the laser beams. For the larger pitch value, no dependence on the Mo NP width is observed. This analysis suggests that the second-order nonlinear response of the core-shell Mo/MoS₂ NPs could be adjusted by suitable choices of the Mo NP width and the pitch size. Comparable results are obtained from shorter sulfurization times, specifically 5 min, as shown by Figure S6, Supporting Information. While in such case the core/shell ratio is different as compared to the longer sulfurization times, as shown in the Figures S7 and S8, Supporting Information, the overall nonlinear response appears to be comparable.

The origin of the reported nonlinear response is further elucidated in Figure 5e. It displays the outcome of a raster scan, consisting of a false color map of the intensity of the SFG nonlinear signal, acquired over an Mo/MoS₂ NP array with pitch value of 1500 nm, Mo NP diameter of 300 nm, and 10 min of sulfurization time. The contributions from the individual NPs are clearly distinguished, though their intensities may differ in some cases. Figure 5e highlights how the nonlinear response of the Mo/MoS₂ NPs, entirely generated by the MoS₂ shells, can be precisely localized at the wafer scale by means of the parameters of the original Mo NP array, such as the pitch.

Having established that the Mo/MoS₂ core-shell NPs exhibit a nonlinear optical response comparable to that of horizontal flakes with the advantage of strong localization, a follow up publication will study in detail how this nonlinear response varies with respect to parameters such as the shell thickness and the cross-sectional geometry.

3. Conclusion

In this work, we have demonstrated for the first time the feasibility of the fabrication of regular arrays of high-yield vertically aligned 1D MoS₂ nanopillars with detailed control on their size, morphology, and position on the wafer. Our approach is based on the combination of top-down (nanofabrication of Mo NPs as scaffolds via lithography and cryo-etching) and bottom-up (sulfurization via CVD) methods, and used to realise 1D core-shell NPs composed by a Mo metal core and a MoS₂ shell. By varying the fabrication and growth parameters, such as the

distance between the Mo NPs and the sulfurization time, we can select the pitch between the Mo/MoS₂ NPs, their cross-sectional shape, and the thickness of the MoS₂ shell among other parameters.

The resultant Mo/MoS₂ NPs are then extensively characterized using SEM and HR-TEM measurements carried out on FIB cross-sections and complemented by the compositional information provided by EELS and Raman spectroscopy measurements. We confirm the structural nature of the as-fabricated Mo/MoS₂ NPs and demonstrate how the MoS₂ layers grow perpendicularly to the sidewalls of the Mo NP core. This is in contrast with previous studies in the literature, where individual NPs or nanowires exhibiting a MoS₂ shell are found to have their layers parallel to the sidewalls,^[15] and hence surrounding the core. Our configuration thus benefits from the marked increase in the number of exposed edge sites, which is known to be advantageous for many applications due to the high reactivity that they exhibit.^[30,31] Furthermore, the nonlinear optical response of the Mo/MoS₂ NPs is established, demonstrating the presence of second-order signal generated by the MoS₂ shell of individual NPs which is highly localized at the wafer scale.

The results of this work demonstrate that vertical core-shell 1D nanostructures can also be fabricated with TMD materials with a high degree of morphology- and position-control. While here we have considered Mo/MoS₂ NPs as a proof-of-concept, our approach is fully general and can be deployed for other TMD materials such as WS₂. In the same manner as traditional semiconductor (e.g., GaAs/AlGaAs^[32,33] or Ge/Si^[12]) core-shell nanowires led to an explosion of applications from optoelectronics to energy harvesting, we foresee that also TMD-based 1D nanostructures could play a key role as building blocks of a new generation of sensors, hydrogen evolution reactions, and optoelectronic devices.

4. Experimental Section

Sulfurization of the Mo-NPs: The sulfurization was carried out in a gradient tube furnace from Carbolite Gero with Argon as the carrier gas. The Ar flow was set up to 150 sccm for all the growths presented in this work. The wafer containing the Mo NPs was placed in the middle zone and gradually heated up to the reaction temperature. Once the sample reached the desired temperature, 400 mg of sulfur placed upstream from the sample was heated up to 220°C.

Cross-Section Sample Preparation for TEM Inspection: The cross-sectional lamellas and cross-section SEM micrographs were prepared using a FEI Helios G4 CX focus ion beam milling system. For the cross-sectional lamellas, a protective Pt layer of 1 μ m in thickness was deposited on top of the NPs arrays at a beam voltage of 30 kV and an ion beam current of 43 pA. The same ion beam current was used for creating the cross-sections.

Scanning Electron Microscopy Inspection: SEM micrographs were acquired in the Helios system at a beam voltage of 10 kV and beam current of 86 pA. Additionally, SEM micrographs were taken in a FEI NovaNano SEM system at a beam voltage of 5 kV and beam current of with a spot size of 3.5.

Transmission Electron Microscopy Measurements: The high-resolution transmission electron microscopy images displayed in Figure 4 were collected in an ARM200F Mono-JEOL microscope operated at 200 kV in TEM mode. In all these images, a spot of size 3 was used; the monochromator was activated without any slit. The electron energy-loss spectral image (EELS-SI) shown in Figure 6, Supporting Information, was also recorded in the same microscope using the STEM mode. The

monochromator was set up on with a slit of 0.1 μm inserted. A probe size of 6C, a CL2 aperture of 30 μm , and a camera length of 12 cm were employed. The EELS-SI was recorded using a Gatan GIF Continuum spectrometer with dispersion of 0.015 eV ch^{-1} , the aperture of the GIF was set to 5 mm, and the pixel time was 1.3 s.

Nonlinear Optical Measurements: The specimen was illuminated with two synchronized laser pulses with wavelengths of $\lambda_1 = 775 \text{ nm}$ and $\lambda_2 = 1200 \text{ nm}$ that were temporally and spatially overlapped. The laser pulses were generated by a femtosecond laser oscillator (Tsunami, Spectra-Physics) and an optical parametric oscillator (OPAL, Spectra-Physics). Both laser beams were focused onto the sample using a microscope objective (Olympus UP-LSAPO 40 \times /0.95), which also collects the emitted light originated through the nonlinear laser-NPs interaction. The collected light was filtered and imaged onto the slit of a spectrometer (PI, Spectra Pro 2300I) using a high-sensitivity cooled CCD camera.

Supporting Information

Supporting Information is available from the Wiley Online Library or from the author.

Acknowledgements

M.B. and S.C.-B. acknowledge financial support from ERC through the Starting Grant "TESLA" grant agreement no. 805021. L.M. acknowledges support from the Netherlands Organizational for Scientific Research (NWO) through the NanoFront program. M.N. and L.K. acknowledge funding in the framework of FP7 Ideas: European Research Council (ERC 340438-CONSTANS).

Conflict of Interest

The authors declare no conflict of interest.

Author Contributions

L.M. developed the fabrication strategy of the Mo NPs. M.B. carried out the sulfurization of the Mo NPs. L.M. performed the FIB milling and the SEM inspection of the samples. S.C.-B. carried out the TEM and EELS measurements. L.M. and S.C.-B. analyzed the TEM data. L.M. prepared Figures 1, 2, and 3; S.C.-B. edited Figure 4; and M.N. prepared Figure 5 and the discussion of the results. S.C.-B. supervised the experiments. All the authors contributed to the discussion and editing of the manuscript. All authors reviewed the manuscript prior to submission.

Data Availability Statement

The data that support the findings of this study are available on request from the corresponding author.

Keywords

2D materials, cryo-etching, Mo/MoS₂ core-shell nanostructures, nanopillar arrays, nonlinear optics, sum frequency generation, transmission electron microscopy

Received: September 2, 2021

Revised: October 5, 2021

Published online:

- [1] P. K. Sahoo, R. Janissen, M. P. Monteiro, A. Cavalli, D. M. Murillo, M. V. Merfa, C. L. Cesar, H. F. Carvalho, A. A. de Souza, E. P. A. M. Bakkers, M. A. Cotta, *Nano Lett.* **2016**, *16*, 4656. PMID: 27336224.
- [2] V. Gautam, S. Naureen, N. Shahid, Q. Gao, Y. Wang, D. Nisbet, C. Jagadish, V. R. Daria, *Nano Lett.* **2017**, *17*, 3369. PMID: 28437614.
- [3] D. J. Carrad, A. B. Mostert, A. R. Ullah, A. M. Burke, H. J. Joyce, H. H. Tan, C. Jagadish, P. Krogstrup, J. Nygård, P. Meredith, A. P. Micolich, *Nano Lett.* **2017**, *17*, 827. PMID: 28002672.
- [4] J. Zhou, S. Deng, L. Gong, Y. Ding, J. Chen, J. Huang, J. Chen, N. Xu, Z. L. Wang, *J. Phys. Chem. B* **2006**, *110*, 10296. PMID: 16722732.
- [5] M. P. Zach, K. H. Ng, R. M. Penner, *Science* **2000**, *290*, 2120.
- [6] Y. Bi, J. Ye, *Chem. Commun.* **2009**, 6551.
- [7] P. Chen, T. Zhou, M. Chen, Y. Tong, N. Zhang, X. Peng, W. Chu, X. Wu, C. Wu, Y. Xie, *ACS Catal.* **2017**, *7*, 7405.
- [8] Y. Kim, H. J. Joyce, Q. Gao, H. Hoe Tan, C. Jagadish, M. Paladugu, J. Zou, A. A. Suvorova, *Nano Lett.* **2006**, *6*, 599.
- [9] M. Heiss, E. Russo-Averchi, A. Dalmau-Mallorquí, G. Tütüncüoğlu, F. Matteini, D. Rüffer, S. Conesa-Boj, O. Demichel, E. Alarcon-Lladó, A. Fontcuberta i Morral, *Nanotechnology* **2013**, *25*, 014015.
- [10] S. Conesa-Boj, F. Boioli, E. Russo-Averchi, S. Dunand, M. Heiss, D. Rüffer, N. Wyrsch, C. Ballif, L. Miglio, A. Fontcuberta i Morral, *Nano Lett.* **2014**, *14*, 1859.
- [11] F. Schuster, J. Kapraun, G. N. Malheiros-Silveira, S. Deshpande, C. J. Chang-Hasnain, *Nano Lett.* **2017**, *17*, 2697.
- [12] S. Conesa-Boj, A. Li, S. Koelling, M. Brauns, J. Ridderbos, T. T. Nguyen, M. A. Verheijen, P. M. Koenraad, F. A. Zwanenburg, E. P. A. M. Bakkers, *Nano Lett.* **2017**, *17*, 2259.
- [13] N. I. Goktas, V. G. Dubrovskii, R. R. LaPierre, *J. Phys. Chem. Lett.* **2021**, *12*, 1275.
- [14] N. Choudhary, C. Li, H.-S. Chung, J. Moore, J. Thomas, Y. Jung, *ACS Nano* **2016**, *10*, 10726. PMID: 27732778.
- [15] Z. Chen, D. Cummins, B. N. Reinecke, E. Clark, M. K. Sunkara, T. F. Jaramillo, *Nano Lett.* **2011**, *11*, 4168.
- [16] D. R. Cummins, U. Martinez, R. Kappera, D. Voiry, A. Martinez-Garcia, J. Jasinski, D. Kelly, M. Chhowalla, A. D. Mohite, M. K. Sunkara, G. Gupta, *J. Phys. Chem. C* **2015**, *119*, 22908.
- [17] D. Zhu, H. Shu, F. Jiang, D. Lv, V. Asokan, O. Omar, J. Yuan, Z. Zhang, C. Jin, *npj 2D Mater. Appl.* **2017**, *1*, 8.
- [18] X. Zhang, H. Nan, S. Xiao, X. Wan, X. Gu, A. Du, Z. Ni, K. (Ken) Ostrikov, *Nat. Commun.* **2019**, *10*, 598.
- [19] C. Tan, H. Zhang, *Nat. Commun.* **2015**, *6*, 7873.
- [20] Q. Liu, X. Li, Z. Xiao, Y. Zhou, H. Chen, A. Khalil, T. Xiang, J. Xu, W. Chu, X. Wu, J. Yang, C. Wang, Y. Xiong, C. Jin, P. M. Ajayan, L. Song, *Adv. Mater.* **2015**, *27*, 4837.
- [21] Y. Chen, B. Song, X. Tang, L. Lu, J. Xue, *Small* **2014**, *10*, 1536.
- [22] M. Bolhuis, J. Hernandez-Rueda, S. E. van Heijst, M. Tinoco Rivas, L. Kuipers, S. Conesa-Boj, *Nanoscale* **2020**, *12*, 10491.
- [23] D. Kong, H. Wang, J. J. Cha, M. Pasta, K. J. Koski, J. Yao, Y. Cui, *Nano Lett.* **2013**, *13*, 1341. PMID: 23387444.
- [24] L. Maduro, C. de Boer, M. Zuiddam, E. Memisevic, S. Conesa-Boj, *Phys. E* **2021**, *134*, 114903.
- [25] B. Ji, Y. E. Panfil, N. Waiskopf, S. Remennik, I. Popov, U. Banin, *Nat. Commun.* **2019**, *10*, 2.
- [26] J. Zhao, B. Chen, F. Wang, *Adv. Mater.* **2020**, *32*, 2004142.
- [27] L. M. Malard, T. V. Alencar, A. P. M. Barboza, K. F. Mak, A. M. de Paula, *Phys. Rev. B* **2013**, *87*, 201401.
- [28] G. Wang, X. Marie, I. Gerber, T. Amand, D. Lagarde, L. Bouet, M. Vidal, A. Balocchi, B. Urbaszek, *Phys. Rev. Lett.* **2015**, *114*, 097403.
- [29] N. Kumar, S. Najmaei, Q. Cui, F. Ceballos, P. M. Ajayan, J. Lou, H. Zhao, *Phys. Rev. B* **2013**, *87*, 161403.

- [30] T. F. Jaramillo, K. P. Jørgensen, J. Bonde, J. H. Nielsen, S. Horch, I. Chorkendorff, *Science* **2007**, 317, 100.
- [31] D. R. Cummins, U. Martinez, R. Kappera, D. Voiry, A. Martinez-Garcia, J. Jasinski, D. Kelly, M. Chhowalla, A. D. Mohite, M. K. Sunkara, G. Gupta, *J. Phys. Chem. C* **2015**, 119, 22908.
- [32] B. Mayer, D. Rudolph, J. Schnell, S. Morkötter, J. Winnerl, J. Treu, K. Müller, G. Bracher, G. Abstreiter, G. Koblmüller, J. J. Finley, *Nat. Commun.* **2013**, 4, 2931.
- [33] G. Koblmüller, B. Mayer, T. Stettner, G. Abstreiter, J. J. Finley, *Semicond. Sci. Technol.* **2017**, 32, 053001.